AIAA JOURNAL
Vol. 36, No. 8, August 1998

K–ϵ and Reynolds Stress Turbulence Model Comparisons for Two-Dimensional Injection Flows

Clarence F. Chenault* and Philip S. Beran†
U.S. Air Force Institute of Technology, Wright–Patterson Air Force Base, Ohio 45433

Two-dimensional steady flowfields generated by transverse injection into a supersonic flow are numerically simulated by integrating the Favré-averaged Navier–Stokes equations. Fine-scale turbulence effects are modeled with compressible K–ϵ and second-order Reynolds-stress turbulence models. These numerical results are compared to numerical results of the Jones–Launder K–ϵ model and experimental data. The credibility of the Reynolds-stress turbulence model relative to experimental data and other turbulence models is demonstrated by comparison of surface pressure profiles, boundary-layer separation location, jet plume height, and descriptions of recirculation zones and flow structure upstream and downstream of the jet. Results indicate that the Reynolds-stress turbulence model correctly predicts mean flow conditions for low static pressure ratios. However, it is also observed that, as the static pressure ratio increases, the boundary-layer separation point moves farther upstream of the jet and predictions become less consistent with experimental results. The K–ϵ results are less consistent with the experimental results than those associated with the Reynolds-stress turbulence model. Finally, unlike the K–ϵ results, nonphysical vorticity phenomena upstream of the jet plume are not observed in the Reynolds-stress turbulence model results. This phenomenon is shown to coincide with strong gradients in the wall functions used to compute μ_t.

Nomenclature

$C_1, C_2, C_s, C_\epsilon, C_{\epsilon_1}, C_{\epsilon_2}, C_\mu, C_w$	= turbulence model closure coefficients
D^t, D^v	= turbulent and viscous diffusion
D_ϵ, D^t_ϵ	= dissipation-rate destruction and diffusion
D^v_ϵ	= viscous diffusion of dissipation rate
E	= specific total energy
e	= specific internal energy
$\boldsymbol{F}, \boldsymbol{G}, \boldsymbol{H}$	= flux vectors
f_{w_1}, f_{w_2}, f_μ	= turbulence model wall damping functions
H	= specific total enthalpy
h	= plumb height, specific internal enthalpy
i, j	= grid dimension
J	= transformation Jacobian
K	= turbulence kinetic energy
l	= length from plate leading edge to jet center
$\boldsymbol{M}$	= Mach number
M_{ij}	= mass flux variation
n	= normal to surface
n_i	= unit normal vector
P_{ij}, P_ϵ	= turbulent and dissipation production
Pr, Pr_t	= Prandtl number and turbulent Prandtl number
p	= static pressure
$\boldsymbol{Q}$	= vector of conserved quantities
q_i	= heat transfer rate per unit area in index notation
Re, Re_t	= Reynolds number and turbulent Reynolds number
$\boldsymbol{S}$	= source term vector
S_{ij}	= strain-rate tensor components
T	= temperature
TI	= turbulence intensity
t	= time
u, v, w	= velocity components
u_i	= velocity in index notation
u_τ	= friction velocity
x, y, z	= rectangular Cartesian coordinates
x_i	= position vector in tensor notation
x_{sep}	= separation length
y^+	= dimensionless, sublayer-scaled distance
$\alpha_1, \alpha^*, \beta_1, \gamma_1$	= turbulence model closure coefficients
γ	= ratio of specific heats
$\Delta x, \Delta y$	= computational mesh step sizes
δ	= boundary-layer thickness
δ_{ij}	= Kronecker delta
ϵ	= turbulence dissipation rate
ϵ_{ij}	= turbulence dissipation rate tensor components
ϵ^w_{ij}	= near-wall correction term to the dissipation rate transport equation
η, ζ	= dimensionless coordinates
κ	= thermal conductivity coefficient
λ	= second bulk viscosity coefficient
μ	= first bulk viscosity coefficient, molecular viscosity
μ_t	= turbulent eddy viscosity
ν	= kinematic viscosity
ξ	= dimensionless coordinate, near-wall correction term
Π_{ij}	= velocity-pressure-gradient correlation tensor
ρ	= density
$\sigma, \sigma_\epsilon, \sigma_\kappa$	= turbulence model closure coefficients
σ_{ij}	= shear-stress tensor components
τ_{ij}	= Favre-averaged Reynolds-stress tensor components
τ_w	= shear stress at the wall
$\phi_{ij,1}, \phi_{ij,2}, \phi^R_{ij}, \phi^w_{ij}$	= velocity pressure-gradient terms
Ψ	= extra production term
ω_z	= z component of vorticity

Subscripts

i, j, k	= tensor indices
jet	= jet quantity
t	= stagnation value, turbulent value
wall	= wall value
∞	= freestream or undisturbed value

Received Sept. 2, 1997; revision received April 2, 1998; accepted for publication April 17, 1998. This paper is declared a work of the U.S. Government and is not subject to copyright protection in the United States.

*Graduate Research Assistant; currently Airframe Integration Engineer, U.S. Air Force Research Laboratory, Air Vehicles Directorate, Aeromechanics Division. Senior Member AIAA.

†Adjunct Associate Professor, Department of Aeronautics and Astronautics. Senior Member AIAA.

Superscripts

$(\cdot^*)$	= sonic condition
$(\tilde{\cdot})$	= mean value of Favre-averaged variable
$(\cdot'')$	= fluctuating value of Favre-averaged variable
$(\bar{\cdot})$	= mean value of Reynolds-averaged variable, time average of any variable
$(\cdot')$	= fluctuating value of Reynolds-averaged variable
$(\hat{\cdot})$	= denotes division by J

I. Introduction

LIMITED computational resources have historically confined simulations with Reynolds-stress turbulence models (RSTMs) to very simple geometries with flowfields only slightly more complex than a fully turbulent flat plate. However, improved computational resources have sparked renewed interest in application of RSTMs to more complex flowfields. One such flowfield currently under investigation is injection of a secondary supersonic jet into a primary supersonic core. This flowfield is encountered in scramjet combustors,[1] rocket motor thrust vector regulation systems,[2] and high-speed flight vehicle reaction control jets.[2] Although this flowfield has been numerically simulated in two dimensions with eddy viscosity models by Rizzetta,[2] Gerlinger et al.,[3] and others, there are inherent physical characteristics (i.e., three-dimensional effect, secondary fluid motion, and rotational fluid movement) that two-equation, eddy viscosity models cannot adequately model.[4] However, second-order RSTMs are not hampered by an eddy viscosity simulation of the Reynolds shear stresses. In an RSTM, shear stresses are treated as conserved variables and modeled with transport equations capable of capturing flowfield characteristics not possible with an eddy viscosity model. Thus, it is assumed that simulations with RSTMs provide more physically realistic predictions than those obtained with an eddy viscosity model.

The RSTM used in this study is the second-order RSTM put forth by Zhang et al.[5] (ZSGS). This model has been validated for fully turbulent flat plate flowfields by Zhang et al.[5] and for flow past a compression ramp by Morrison et al.[6] Morrison et al. reported favorable comparisons of predictions made with a two-dimensional grid to experimental results from Settles and Dodson[7] for ramp angles of 8 and 16 deg. However, at a 20-deg ramp angle the model begins to fail. Morrison et al.[6] attribute the failure at 20 deg to three-dimensional interactions not accounted for by the two-dimensional grid.

The present investigation attempts to validate the ZSGS RSTM for a flowfield with injection of a secondary supersonic jet into a primary supersonic core. This will be accomplished by numerically simulating the slot injection experiments of Spaid and Zukoski[8] and Aso et al.[9] with the ZSGS RSTM and comparing the ZSGS RSTM predicted values with experimental data and predicted values from a $K-\epsilon$ model contracted from the ZSGS RSTM and the Jones–Launder[10] $K-\epsilon$ model.

A typical two-dimensional flowfield generated by sonic injection is characterized in Fig. 1. Injection occurs normal to the freestream, and the underexpanded jet has sonic conditions over most of the nozzle exit. The underexpanded gas leaving the nozzle penetrates the turbulent boundary layer, setting up a system of shock and recirculation regions fore and aft of the nozzle. In the inviscid region upstream of the jet, a jet-induced bow shock forms due to blockage of the flow, and the subsequent adverse pressure gradient causes boundary-layer separation. In the region immediately upstream of the jet, a recirculation region consisting of counter-rotating primary and secondary upstream vortices (PUV and SUV, respectively) are present. For some of the cases examined, there is also a tertiary upstream vortex formed between the surface of the plate and the PUV. The boundary-layer displacement of the vortices causes a separation shock to form upstream of the recirculation region. Between the recirculating region and the separation shock is a sonic surface that has flow displacement characteristics similar to a compression ramp in a supersonic flow. Upon exiting the nozzle, expansion of the jet is followed by a rapid decrease in the local pressure. This results in a normal shock, and thus a sonic surface and a Mach disk form surrounding the jet plume. Downstream of the jet, the flow is turned parallel to the surface, producing a recompression shock and a corresponding separated, recirculation region behind the nozzle consisting of counter-rotating primary and secondary downstream vortices (PDV and SDV, respectively).

The effects of the primary and secondary vortices upstream and downstream of the jet are clearly seen in the five distinct regions of the surface static-pressure profile (see inset of Fig. 1). Spaid and Zukoski[8] report a steep pressure rise (region 1) as a result of boundary-layer separation, followed by a flattening or plateauing of the pressure upstream of the jet (region 2). The behavior of the pressure in region 2 is a result of the relatively constant flow conditions of the PUV. The pressure plateau is followed by a pressure spike (region 3) caused by the SUV. Immediately downstream of the jet is a large pressure well (region 4) with two subregions contained therein. The first subregion is a slight pressure rise caused by the leading edge of the PDV. The second subregion is a pressure drop caused by the SDV. The pressure well is followed by a pressure hump (region 5) associated with the trailing edge of the PDV, boundary-layer reattachment, and the recompression shock.

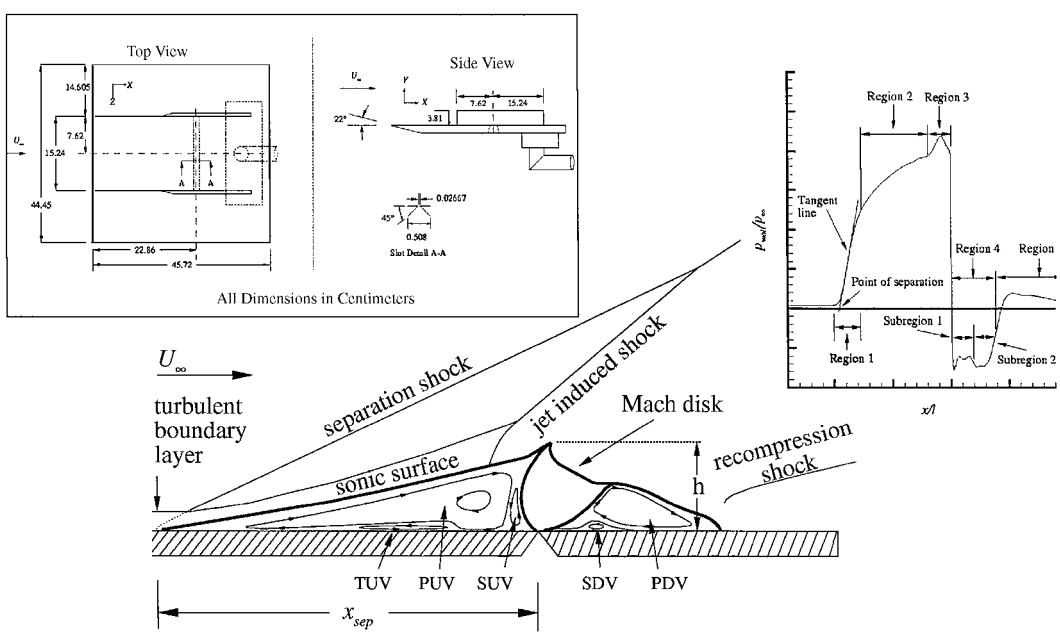

Fig. 1 Schematic of slot injection flowfield.

Spaid and Zukoski[8] also report that without the end plates at the ends of the slot (see inset of Fig. 1) there are significant three-dimensional effects. The three-dimensional relaxation of the flow results in reduced maximum values of the surface static pressure and causes the upstream separation point to move closer to the jet.

The two-dimensional flowfield just described has many similarities to flow past a forward-facing step and to flow over a compression ramp.[8] Data presented by Sterrett and Holloway[11] indicate that if the step height and jet penetration distance are adjusted so that the separation lengths of the separated regions are approximately the same, the two-dimensional separated flowfield produced by a forward-facing step is the same as the upstream separated flowfield produced by a jet. Spaid and Zukoski[8] report that shock boundary-layer structures seen upstream of the jet-induced separation region are similar to those seen in compression ramps. Furthermore, they state that, for the cases examined, they found the angle of the sonic surface is $\approx$13 deg and the pressure rise near the separation point corresponds to the pressure rise that occurs when an inviscid flow is turned through the same angle. Thus, the sonic surface is analogous to the surface of a compression ramp with a turbulent boundary layer on its surface.

A schematic of Spaid and Zukoski's[8] experimental apparatus is shown in the inset of Fig. 1. The apparatus consisted of a flat plate with a sharp leading edge located a distance $l = 22.86$ cm upstream of the centerline of the nozzle placed in a wind-tunnel test section 51-cm wide. A sonic jet of gas was injected normal to the primary flowfield through the throat of a nozzle 0.02667 cm wide and 15.24 cm long in the transverse direction. A 14.6-cm gap was left between the end of the slot and the tunnel wall. End plates with glass inserts were mounted on either side of the slot to help ensure two-dimensionality. The experiments were conducted with a test section Mach number of 3.50. Measured quantities consisted of test section flow parameters, jet reservoir flow parameters, and static-pressure distributions at the surface of the plate around the jet. Shadowgraphs and surface static-pressure profiles indicated the flow was fully turbulent upstream of the jet and free of shocks between the plate leading edge and the separation shock.

Aso et al.[9] used a similar experimental configuration to conduct their experiments. Their configuration consisted of a flat plate with a sharp leading edge located $l = 33.0$ cm upstream of the centerline of the nozzle in a 15×15 cm test section operating at Mach 3.75. They also injected a sonic jet of gas normal to the external flow through the surface of the model. Nozzle throats measuring 0.5 and 1.0 mm were used, and both nozzles had transverse lengths of 13.0 cm. This length left a gap of 1.0 cm between the nozzle and the test section wall on both sides of the nozzle. Measured quantities consisted of test section flow parameters, jet reservoir flow parameters, static-pressure distributions at the surface of the plate around the jet, jet penetration height h, and boundary-layer separation distance from the jet x_{sep} (see Fig. 1).

Numerical calculations were performed by Rizzetta[2] to simulate the Aso et al.[9] flowfield described earlier. Rizzetta used the Jones–Launder[10] K–ϵ model with Sarkar[12] compressibility correction to model the compressible turbulent dissipation in the kinetic energy equation. Furthermore, the numerical solver Rizzetta used did not include K in the total energy equation. Rizzetta reported relatively good agreement with the experimental surface pressure in regions 1 and 2 but always overpredicted the peak pressure in region 3.

Observations about the effectiveness of the Jones–Launder K–ϵ model used by Rizzetta may be misleading because there are a number of deficiencies in the Aso et al.[9] data set. These deficiencies are evident from the surface static-pressure profiles (see Fig. 10 of Ref. 9). The number of pressure taps was insufficient to capture the pressure spike upstream of the jet or the pressure well downstream of the jet. Additionally, the choppy nature of the static-pressure distributions upstream of the separation point suggests the flow leading up to the jet is unstable or that there are some shock/boundary-layer interactions elsewhere on the plate. These deficiencies, combined with the lack of end plates to ensure two-dimensionality of the flow, renders this data set less than ideal for turbulence model validation.

A more suitable data set for model validation is data obtained by Spaid and Zukoski.[8] This data set has very smooth and consistent pressure profile data, and enough pressure taps were used to capture the pressure spike upstream of the jet and the pressure well downstream of the jet. Furthermore, two-dimensionality of the flow was enhanced by the addition of end plates on both sides of the jet slot.

II. Governing Equations

The governing equations for the compressible turbulent flow of an ideal gas, with bulk viscosity, body forces, and real gas effects neglected, are assumed to be the unsteady, compressible, Favre-averaged Navier–Stokes (FANS) equations[13]:

$$\bar{\rho}_{,t} + (\bar{\rho}\tilde{u}_k)_{,k} = 0 \tag{1}$$

$$(\bar{\rho}\tilde{u}_i)_{,t} + (\bar{\rho}\tilde{u}_i\tilde{u}_k + \bar{p}\delta_{ik})_{,k} - (\tilde{\sigma}_{ik} - \bar{\rho}\tau_{ik})_{,k} = 0 \tag{2}$$

$$(\bar{\rho}\tilde{E})_{,t} + (\bar{\rho}\tilde{u}_k\tilde{H})_{,k} - \left(D^v_{ii} + D^t_{iik} + \tilde{u}_i\tilde{\sigma}_{ik} - \bar{\rho}\tilde{u}_i\tau_{ik} - \tilde{q}_k + \overline{u''_i}\tilde{\sigma}_{ik} - C_p\bar{\rho}\overline{u''_k T''}\right)_{,k} = 0 \tag{3}$$

where $(\cdot)_{,*}$ indicates a derivative with respect to time or the spatial coordinate x_i. Furthermore, $\tilde{E} \equiv \tilde{e} + \frac{1}{2}\tilde{u}_i\tilde{u}_i + K$ is the specific total energy, $\tilde{H} \equiv \tilde{h} + \frac{1}{2}\tilde{u}_i\tilde{u}_i + K$ is the specific total enthalpy, $\tilde{\sigma}_{ik} = 2\bar{\mu}\tilde{S}_{ik} + \bar{\lambda}\tilde{S}_{jj}\delta_{ik}$ are the components of the shear-stress tensor where by Stokes hypothesis $\lambda = -\frac{2}{3}\mu$, $\tilde{S}_{ik} = \frac{1}{2}(\tilde{u}_{i,k} + \tilde{u}_{k,i})$ are the components of the strain-rate tensor, $\tilde{q}_k = -\kappa\tilde{T}_{,k}$ is the convective heat flux, $D^v_{ii} = \overline{u'_i\sigma'_{ik}}$ is the viscous diffusion of turbulent stresses, $D^t_{iik} = -\frac{1}{2}\bar{\rho}\overline{u''_k u''_i u''_i}$ is the turbulent diffusion of turbulent stresses, $C_p\bar{\rho}\overline{u''_k T''}$ is the Reynolds turbulent heat flux, $K = \tau_{ii}/2$ is the turbulent kinetic energy, and $\tau_{ik} = \overline{u'_i u'_k}$ are the Favre-averaged Reynolds-stress tensor components (RSTC). This definition of τ_{ik} is adopted to maintain consistency with sources and software cited from the NASA Langley Research Center, although the more common definition is $\tau_{ik} = -\overline{\rho u''_i u''_k}$.

In addition to the turbulence models, an equation of state must be specified for system closure. The perfect gas equation of state used for this study is

$$\bar{p} = \bar{\rho}(\gamma - 1)\left(\tilde{E} - \tilde{u}_i^2/2 - K\right) \tag{4}$$

where γ is the ratio of specific heats.[14] The presence of K in Eq. (4) (a result of the Favre-averaging process) creates a strong coupling between the FANS equations and the turbulence transport equations.

A. Second-Order Model

Second-order turbulence models are assumed to capture more of the true physical nature of a flowfield because they allow direct computation of the RSTC. Therefore, expressions for the computation of the RSTC must be developed. The Favre-averaged Reynolds-stress transport equations are found in many sources, Refs. 5, 15, and 16, and are given as

$$(\bar{\rho}\tau_{ij})_{,t} + (\bar{\rho}\tilde{u}_k\tau_{ij})_{,k} = D^v_{ij,k} + D^t_{ijk,k} + P_{ij} - \bar{\rho}\epsilon_{ij} + \Pi_{ij} + M_{ij} \tag{5}$$

The terms in Eq. (5) as modeled by the ZSGS RSTM[5] are given as

$$D^v_{ij} = \overline{\sigma'_{ik}u'_j} + \overline{\sigma'_{jk}u'_i} \cong \bar{\mu}(\tau_{ij,k} + \tau_{jk,i} + \tau_{ik,j}) \tag{6}$$

$$D^t_{ijk} = -\bar{\rho}\overline{u''_i u''_j u''_k} \cong \bar{\rho}C_s(K/\epsilon)(\tau_{ij,k} + \tau_{jk,i} + \tau_{ik,j}) \tag{7}$$

$$P_{ij} = -\bar{\rho}\tau_{ik}\tilde{u}_{j,k} - \bar{\rho}\tau_{jk}\tilde{u}_{i,k} \tag{8}$$

$$\epsilon_{ij} = \overline{\sigma'_{ik}u'_{j,k}} + \overline{\sigma'_{jk}u'_{i,k}} \cong \tfrac{2}{3}\epsilon\delta_{ij} + \epsilon^w_{ij}/\bar{\rho} \tag{9}$$

$$\Pi_{ij} = (\overline{p'u'_{i,j}} + \overline{p'u'_{j,i}}) - (\overline{p'u'_i}\delta_{jk} + \overline{p'u'_j}\delta_{ik})_{,k} \cong \phi_{ij,1} + \phi_{ij,2} + \phi^R_{ij} + \phi^w_{ij} \tag{10}$$

$$M_{ij} = \overline{u''_i}(\bar{\sigma}_{jk,k} - \bar{p}_{,j}) + \overline{u''_j}(\bar{\sigma}_{ik,k} - \bar{p}_{,i}) \cong 0 \tag{11}$$

The two parts of the velocity-pressure-gradient correlation tensor are often referred to separately as the pressure strain rate and the pressure diffusion. Zhang et al.[5] invokes Morkovin's[17] hypothesis to eliminate the mass flux variation term M_{ij}. As stated by Wilcox,[4]

"Morkovin hypothesized that the effects of density fluctuations on the turbulence are small provided they remain small relative to the mean density."

Zhang et al.[5] put forth models for the velocity-pressure-gradient correlation and dissipation rate tensor as $\Pi_{ij} = \phi_{ij,1} + \phi_{ij,2} + \phi_{ij}^R + \phi_{ij}^w$, where $\phi_{ij,1} + \phi_{ij,2}$ is the high-Reynolds-number model of Launder et al.[17] (LRR), and ϕ_{ij}^R is the pressure echo term formulated by ZSGS,[5] which is based on the proposal of LRR.[18] The near-wall corrections, ϕ_{ij}^w and ϵ_{ij}^w, were formulated in Refs. 19 and 20. The models for these terms as seen in Ref. 5 are

$$\phi_{ij,1} = -C_1\bar{\rho}(\epsilon/2K)\left(\tau_{ij} - \tfrac{2}{3}K\delta_{ij}\right) \tag{12}$$

$$\phi_{ij,2} = -\alpha_1\left(P_{ij} - \tfrac{1}{3}P_{kk}\delta_{ij}\right) - \beta_1\left(D_{ij} - \tfrac{1}{3}P_{kk}\delta_{ij}\right) - 2\gamma_1\bar{\rho}K\left(S_{ij} - \tfrac{1}{3}S_{kk}\delta_{ij}\right) \tag{13}$$

$$\phi_{ij}^R = 2C_w\bar{\rho}K\left(\tilde{S}_{ij} - \tfrac{1}{3}\tilde{S}_{kk}\delta_{ij}\right)\left(K^{\frac{3}{2}}/\epsilon x_j\right) \tag{14}$$

$$\phi_{ij}^w = f_{w1}\left[C_1\bar{\rho}(\epsilon/K)\left(\tau_{ij} - \tfrac{2}{3}K\delta_{ij}\right) + \alpha^*\left(P_{ij} - \tfrac{1}{3}P_{kk}\delta_{ij}\right) - \bar{\rho}(\epsilon/K)(\tau_{ik}n_kn_j + \tau_{jk}n_kn_i)\right] \tag{15}$$

$$\epsilon_{ij}^w = f_{w1}\left[-\frac{2}{3}\bar{\rho}\epsilon\delta_{ij} + \bar{\rho}\frac{\epsilon}{K}\left(\frac{\tau_{ij} + \tau_{ik}n_kn_j + \tau_{jk}n_kn_i + n_in_j\tau_{kl}n_kn_l}{1 + \frac{3}{2}\tau_{kl}n_kn_l/K}\right)\right] \tag{16}$$

In these expressions, $D_{ij} = -(\bar{\rho}\tau_{ik}\tilde{u}_{k,j} + \bar{\rho}\tau_{jk}\tilde{u}_{k,i})$, and the damping function is given as $f_{w1} = \exp[-(Re_t/150)^2]$, where the turbulent Reynolds number is defined as $Re_t = K^2/(\bar{\nu}\epsilon)$ and the unit normal measured positive from the wall is defined as $n_i = (0, 1, 0)$. Closure constants given in Ref. 5 are $\alpha_1 = (C_2 + 8)/11$, $\beta_1 = (8C_2 - 2)/11$, $\gamma_1 = (30C_2 - 2)/55$, $\alpha^* = 0.45$, $C_1 = 3.0$, $C_2 = 0.4$, and $C_w = (C_w)_{\text{in}} - (5.8 \times 10^{-4})\boldsymbol{M}_\infty$ for $\boldsymbol{M}_\infty > 2.5$ and $(C_w)_{\text{in}} = 0.0153$ for $Re_\theta > 5.5 \times 10^0$, where Re_θ is the Reynolds number based on the momentum thickness θ (Ref. 5).

The dissipation-rate transport equation is derived from the moments of the Reynolds-averaged fluctuating momentum equations. A general form of the dissipation-rate transport equation as found in Refs. 4 and 21 is given as

$$(\bar{\rho}\epsilon)_{,t} + (\bar{\rho}\tilde{u}_k\epsilon)_{,k} = D_{\epsilon,k}^v + D_{\epsilon,k}^t + P_\epsilon - D_\epsilon + \Psi + \xi \tag{17}$$

The customary approach toward development of a dissipation-rate model for compressible flows is to follow Sarkar et al.'s[22] method and partition the dissipation rate into a solenoidal (incompressible) component and a compressible component. Compressibility effects are then represented as asymptotic corrections to the solenoidal dissipation rate, which allows for the direct extension of the incompressible form to compressible flowfields. However, this is inconsistent in the present context where Morkovin's hypothesis has been invoked.

Consistent with the assumptions made with Morkovin's hypothesis, the isotropic dissipation-rate equation models as put forth by Zhang et al.[5] are as follows: $D_\epsilon^v = \bar{\mu}\epsilon_{,k}$, $D_\epsilon^t = C_\epsilon\bar{\rho}(K/\epsilon)\tau_{ik}\epsilon_{,k}$, $P_\epsilon = C_{\epsilon_1}(\epsilon/K)(P_{ii}/2)$, $D_\epsilon = C_{\epsilon_2}\bar{\rho}\epsilon^2/K$, $\Psi = C_{\epsilon_1}\sigma f_{w_2}P_{ii}\epsilon/(2K)$, $\xi = f_{w_2}\bar{\rho}(-2\epsilon\tilde{\epsilon}/K + 1.5\tilde{\epsilon}^2/K)$, $\tilde{\epsilon} = \epsilon - 2\bar{\nu}(\sqrt{K}_{,j})^2$, and $\bar{\epsilon} = \epsilon - 2\bar{\nu}K/x_j^2$. The damping function is defined as $f_{w_2} = \exp[-(Re_t/40)^2]$, and closure constants are given as $C_\epsilon = 0.1$, $C_{\epsilon_1} = 1.5$, $C_{\epsilon_2} = 1.83$, and $\sigma = 1.5$.

Closure of the energy equation is achieved by modeling the turbulent heat flux as[5] $C_p\bar{\rho}\overline{u_k''T''} = -(C_p\mu_t/Pr_t)\tilde{T}_{,k}$, where C_p is the specific heat at constant pressure, and the turbulent Prandtl number Pr_t is 0.9. The turbulent eddy viscosity is defined as

$$\mu_t = \bar{\rho}C_\mu f_\mu(K^2/\epsilon) \tag{18}$$

where $C_\mu = 0.096$ and the damping function is given as[5]

$$f_\mu = \left(1 + 3.45/\sqrt{Re_t}\right)\tanh(y^+/115) \tag{19}$$

where $y^+ = yu_\tau/\bar{\nu}$, the friction velocity is $u_\tau = \sqrt{(\tau_w/\bar{\rho}_w)}$ and

$$\tau_w = \mu\left.\frac{\partial u}{\partial y}\right|_{y=0} \tag{20}$$

is the shear stress at the wall.[23]

B. Two-Equation Model

Two-equation turbulence models have long been a favorite of computational fluid dynamics analysts. However, all two-equation models are limited to an eddy viscosity simulation of the Reynolds shear stresses. Although eddy viscosity models provide adequate results for a limited number of flowfields, they completely break down for many other types of flowfields, including three-dimensional flows, flow in ducts with secondary motions, and flow in rotating fluids.[4] The latter two of these examples apply to the flowfield being considered here.

With the advent of RSTM, two-equation models are often used to provide initial flowfield conditions for more complex turbulence models. The compressible K–ϵ model put forth by Zhang et al.[24] was used for this purpose in this study and to provide a basis of comparison for the higher-order RSTM.

The compressible turbulent kinetic energy transport equation used by Zhang et al.[24] is derived from the contraction of the Reynolds-stress equation reported by Speziale and Sarkar[15]:

$$(\bar{\rho}K)_{,t} + (\bar{\rho}\tilde{u}_kK)_{,k} = D_{ii,k}^v + D_{iik,k}^t + P_{ii} - \bar{\rho}\epsilon_{ii} + \Pi_{ii} + M_{ii} \tag{21}$$

The contracted and simplified forms of Eqs. (8–10) as given by Zhang et al.[24] are $D_{ii}^v = \bar{\mu}K_{,k}$, $D_{iik}^t = (\mu_t/\sigma_\kappa)K_{,k}$, $P_{ii} = -\bar{\rho}\tau_{ik}\tilde{u}_{i,k}$, $\Pi_{ii} = 0$, $\epsilon_{ii} = \epsilon$, and $M_{ii} = 0$ where σ_κ is a constant taken to be 0.75 and the RSTC in the turbulent production term is modeled using the standard eddy viscosity formulation. Zhang et al.[5] give the RSTC as

$$\tau_{ik} = -2(\mu_t/\bar{\rho})\left(\tilde{S}_{ik} - \tfrac{1}{3}\tilde{S}_{jj}\delta_{ik}\right) + \tfrac{2}{3}K\delta_{ik} \tag{22}$$

where μ_t is the eddy viscosity defined in Eq. (18). The mass flux term is assumed to be negligible by Morkovin's hypothesis.[17]

The contraction of the pressure-velocity-gradient correlation is identically zero with the exception of the third term of ϕ_{ij}^w. Thus, Π_{ii} should be modeled as

$$\Pi_{ii} = f_{w_1}\rho\tau_{ik}n_in_k \tag{23}$$

Likewise, ϵ_{ii} should be modeled as

$$\epsilon_{ij} = \epsilon + f_{w_1}\left[-\epsilon + \frac{\epsilon}{2K}\left(\frac{2K + 2\tau_{ik}n_kni + n_in_k\tau_{kl}n_kn_l}{1 + \frac{3}{2}\tau_{kl}n_kn_l/K}\right)\right] \tag{24}$$

However, as has been done with every other K–ϵ model the authors know of, Zhang et al.[5] ignore these terms.

The dissipation-rate transport equation developed for the RSTM is also used for the K–ϵ model; however, for the two-equation model D_ϵ^t is modeled as $(\mu_t/\sigma_\epsilon)\epsilon_{,k}$, where $\sigma_\epsilon = 1.45$ (Ref. 5).

The primary differences between the ZSGS K–ϵ model and the Jones–Launder K–ϵ model used by Rizzetta[2] are the wall functions and the application of Sarkar et al.'s[25] compressibility correction to the dissipation-rate term in the K transport equation.

III. Numerical Solver

The numerical solver used for this study was NASA Langley's integrated solution algorithm for arbitrary configurations (ISAAC).[16] ISAAC is a three-dimensional finite volume program that uses time integration of the governing equations to compute a steady-state solution of the Favre-averaged Navier–Stokes equation. The integration is performed with a spatially split, diagonalized, approximate factorization scheme.[16]

Several two-equation and RSTMs suitable for modeling a variety of flow conditions have been incorporated into ISAAC. However, for supersonic, wall-bounded flows, only the ZSGS K–ϵ model and the ZSGS RSTM are fully operational in the current version of ISAAC.

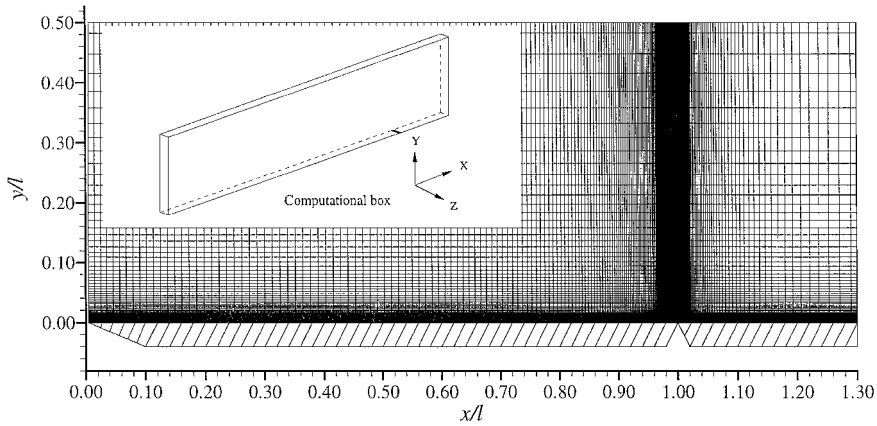

Fig. 2 Computational grid and computational box.

To facilitate gridding of complex geometries, a coordinate transformation to a generalized ξ, η, ζ coordinate system is performed. The transformed governing equations can be represented in vector form as follows:

$$\frac{\partial \hat{\boldsymbol{Q}}}{\partial t} + \frac{\partial(\hat{\boldsymbol{F}} - \hat{\boldsymbol{F}}_v)}{\partial \xi} + \frac{\partial(\hat{\boldsymbol{G}} - \hat{\boldsymbol{G}}_v)}{\partial \eta} + \frac{\partial(\hat{\boldsymbol{H}} - \hat{\boldsymbol{H}}_v)}{\partial \zeta} = \boldsymbol{S} \qquad (25)$$

where

$$\hat{\boldsymbol{Q}} = \boldsymbol{Q}/J = J^{-1}\{\rho, \rho u, \rho v, \rho w, \rho E, \rho\tau_{xx}, \rho\tau_{yy}, \rho\tau_{zz}, \rho\tau_{xy}, \rho\tau_{xz}, \rho\tau_{yz}, \rho\epsilon\}^T \qquad (26)$$

and where $\hat{\boldsymbol{F}}$, $\hat{\boldsymbol{G}}$, and $\hat{\boldsymbol{H}}$ are the corresponding inviscid, or convective, fluxes; $\hat{\boldsymbol{F}}_v$, $\hat{\boldsymbol{G}}_v$, and $\hat{\boldsymbol{H}}_v$ are the viscous or diffusive fluxes; and $\boldsymbol{S}$ represents the source terms due to production, destruction, and redistribution.[26] For notational simplicity, the overbars and tildes are dropped from the mean variables with the understanding that these are Favre-averaged variables. The transformation methodology is also applied to the two-equation model flow.

Second-order spatial accuracy for the inviscid terms is attained by using the MUSCL scheme of van Leer[27] with a generalized form of Roe's approximate Riemann solver[28]; the Venkatakrishnan limiter[29] is used to avoid spurious oscillations in the neighborhood of a discontinuity.

Consistent with the elliptic nature of the diffusive fluxes, finite volume representations of second-order accurate, central-difference operators are employed.[30,31] Derivatives required in the diffusive flux and source term evaluations at the cell interface are approximated with the gradient theorem by integrating around an auxiliary cell centered about the interface. Flow variables required at this interface are obtained from arithmetic averaging of neighboring cell averages.[16]

IV. Boundary Conditions

The computational domain for this study consists of a six-sided rectangular box (see inset of Fig. 2). The lower edge of the domain corresponds to the solid surface of the flat plate with a slot cut in it for the jet, whereas the upper surface corresponds to the top of the wind tunnel. The leftmost plane is the inflow plane, and the rightmost plane is the outflow plane. The two side planes represent either side of the wind-tunnel centerline.

The flow upstream of the flat plate is supersonic. Thus, the leading edge of the plate is taken to be the beginning of the computational domain, and all dependent variables are assigned freestream values. Inflow turbulence quantities for both models are based upon the turbulence intensity of the undisturbed flow. Turbulence intensity is defined as $TI = \sqrt{(2/3K_\infty)}/u_\infty$. The value of TI is generally a well-documented characteristic for a particular wind-tunnel test section. For the K–ϵ model, K_∞ is computed directly from the definition of TI. For the RSTM, τ_{ii} is found by assuming the freestream turbulence is homogeneous and isotropic. Thus, $\tau_{xx_\infty} = \tau_{yy_\infty} = \tau_{zz_\infty} = 2/3K_\infty$, and $\tau_{xy_\infty} = \tau_{xz_\infty} = \tau_{yz_\infty} = 0$. The freestream dissipation rate for both models is commonly found by setting $\mu_{t_\infty} = \mu_\infty$ in Eq. (18) (Refs. 2 and 3).

The boundary condition at the top of the computational domain, representing the upper surface of the wind tunnel, is modeled with Abbett's tangency condition.[32] Tangency permits the reflection shock from the top of the wind tunnel to interact with the rest of the flowfield but does not require the large number of nodes needed to resolve a boundary layer. A first-order extrapolation from the interior is also used to provide boundary conditions for the downstream exit plane and the two side boundaries. On the lower wall, the no-slip condition, $u = v = w = 0$, is invoked, along with $\partial p/\partial n = 0$ and the adiabatic wall condition $\partial T/\partial n = 0$. The homogeneous condition applies to the stresses at the wall such that $K = \tau_{ij} = 0$. To maintain asymptotic consistency of the dissipation-rate equation at the wall, $\epsilon = 2\bar{\nu}(\sqrt{K_{,j}})^2$ is used as the boundary condition for the dissipation-rate equation.

For each case investigated, the total pressure and total temperature of the injected fluid are known, and the converging nozzle is assumed choked. Therefore, the following uniform conditions are applied to all cells except the first three and last three cells across the slot in the plane of the nozzle exit: $p = p^*$, $T = T^*$, $u = w = 0$, and $v = v^*$, where $*$ indicates a choked flow condition. Linear interpolation between the last cell on the plate in front of the jet and the third cell of the interior of the jet is used to smooth the transition from the plate conditions to the jet conditions. A similar procedure is used at the rear of the jet. This is done to simulate the boundary layer of the jet nozzle at the interface of the jet and the plate. Uniform boundary conditions of $\partial K/\partial n = \partial\tau_{ij}/\partial n = \partial\epsilon/\partial n = 0$ are used for the turbulence variables.

V. Results

Results comparing surface static-pressure ratios, boundary-layer separation length, and plume height are gathered for two flow configurations: that of Spaid and Zukoski[8] and of Aso et al.[9] The following conditions characterize the Spaid and Zukoski[8] configuration: freestream Mach number of 3.5, $Re/m = 13.42 \times 10^6$, slot width of 0.2667 mm, and static pressure ratios (p_{jet}/p_∞) ranging from 8.743 to 63.5. These conditions characterize the Aso et al.[9] configuration: freestream Mach number of 3.75, $Re/m = 62.7 \times 10^6$, slot width of 1.0 mm, and static-pressure ratios ranging from 4.86 to 25.15. Table 1 is a summary of the mean flow parameters used during this study. Initially, a grid resolution study is reported, and a comparison of profiles of turbulent shear-stress predictions from the ZSGS RSTM and ZSGS K–ϵ model is presented along with comparisons of contour plots of the shear stresses and vorticity surrounding the jet. Finally, an illustration of the significance of the turbulent kinetic energy as part of the total energy equation is presented.

A. Grid Study

The Aso et al.[9] configuration provided the first data set examined and served as the basis for a grid sensitivity study using the test condition $p_{\text{jet}}/p_\infty = 10.29$. This pressure ratio was used for the grid study because it had the most complete and thermodynamically consistent data. An algebraic, nonuniform, Cartesian mesh with its

Table 1 Summary of mean flow parameters

Parameter	Aso et al.[9]	Spaid and Zukoski[8]
M_∞	3.75	3.5
p_∞, Pa	11,090	3,145
T_∞, K	78.43	86.5
Re/m	62.73×10^6	13.4×10^6
M_{jet}	1.0	1.0
p_{jet}/p_∞	4.86, 10.29, 17.72, 25.15	8.74, 17.12 42.79, 63.50
T_{jet}, K	249	298

origin at the leading edge of the plate and nondimensionalized by the length l was generated using GRIDGEN Version 9 (Ref. 33). The final computational grid consisted of 337×121 nodes in the x and y directions, respectively (see Fig. 2), with the nodes representing cell vertices. The minimum of Δx occurred across the nozzle, where 44 uniformly spaced nodes were used. Streamwise node spacing was increased away from the jet boundaries according to the one-dimensional tanh stretching function of Vinokur.[34] There were 201 nodes upstream of the jet and 94 nodes downstream of the jet. At the leading edge of the domain, the mesh step was $\Delta x/l = 0.01$, and at the trailing edge of the domain, it was $\Delta x/l = 0.192$. In the normal direction, tanh stretching was used to ensure a smooth distribution of the nodes through the boundary layer and out into the freestream. Because low-Reynolds-number terms in the turbulence models are sensitive to grid spacing at solid boundaries, Δy was chosen at the surface such that $y^+ < 1.0$ at the first mesh point above the plate for all grid distributions evaluated. It was found that $\Delta y/l = 0.00001$ satisfied this requirement for all cases examined.

The final grid dimensions ($i \times j$) were determined in two steps. First, the requirements for j were determined by examining the static surface pressure profiles of steady solutions for grid dimensions of 253×81, 253×121, and 253×161. The pressure profiles computed with these three grids are seen in Fig. 3a. It was evident that grid convergence in the normal direction was obtained with the two finest meshes; thus, $j = 121$ was used for the remainder of the grid study. Second, streamwise grid requirements were determined by examining the static surface pressure profiles for grid dimensions of 253×121, 337×121, and 439×121. The pressure profiles computed with these three grids are seen in Fig. 3b. It was evident that grid convergence in the streamwise direction was obtained on the two finest grids. Thus, $i = 337$ was specified in the final construction of the grid used for both physical configurations.

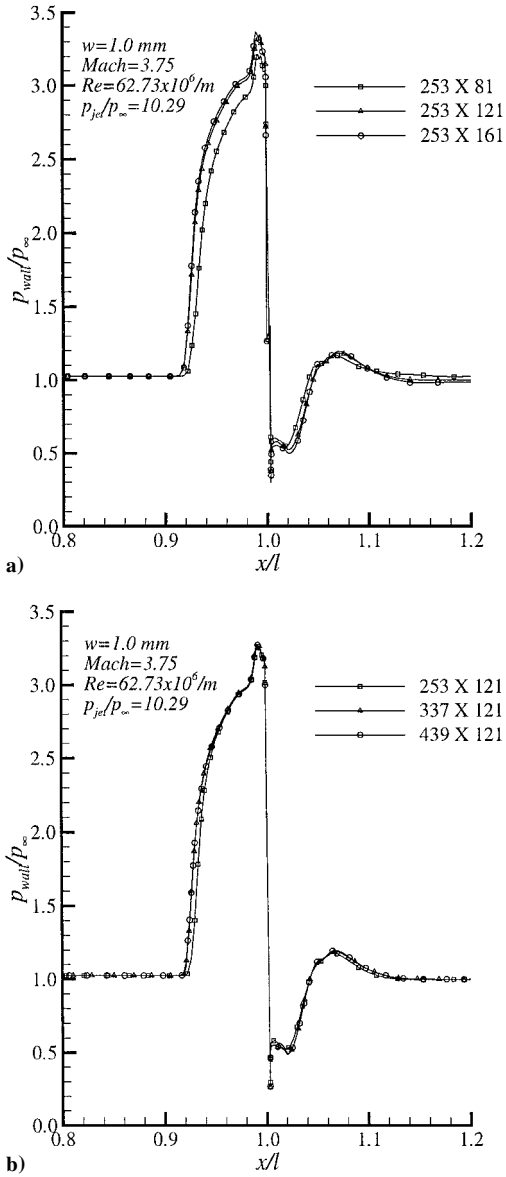

Fig. 3 Pressure profiles used in grid study (Aso et al.[9] configuration).

B. Pressure Profile Data

1. Aso et al. Configuration

Numerical simulations using the two ZSGS turbulence models were performed to simulate Aso et al.'s[9] configuration observing the mean flow conditions listed in Table 1. These results were compared with experimental data and numerical data predicted by the Jones–Launder K–ϵ model as reported by Rizzetta.[2] For the most part, all three models had poor agreement with the experimental data, and much of the disagreement is attributed to the experimental configuration, which likely had three-dimensional effects in the flowfield and strong leading-edge shocks. The supposition of three-dimensional effects is consistent with the results shown by Spaid and Zukoski[8] when the end plates were removed. Specifically, the boundary-layer separation point moves closer to the nozzle and peak pressure in region 3 decreases.

As mentioned in Sec. I, the number of pressure taps used by Aso et al. was insufficient to capture all of the characteristics of the surface pressure profile. As seen in Fig. 4, the pressure rise just upstream of the jet was captured only for the largest static-pressure ratio (25.15), and the pressure well immediately downstream of the jet was completely missing for the smallest static-pressure ratio (4.86). Furthermore, the surface static-pressure ratio upstream of the separation point is not unity. This suggests there may be additional shock/boundary-layer interactions elsewhere on the plate, possibly leading to another separation point further upstream of the jet.

Despite the shortcomings of this data set, flowfield simulations of the four static pressure ratios listed in Table 1 were computed using the ZSGS RSTM and ZSGS K–ϵ models. Resultant surface static-pressure distributions for these simulations were compared with experimental data and Rizzetta's[2] computations with the Jones–Launder K–ϵ model in Fig. 4. The Jones–Launder model[10] had good agreement with the pressure profiles in region 1 at the two higher pressure ratios, whereas simulations with the two ZSGS models had good agreement with the pressure profiles in region 1 at the two lower pressure ratios. All of the models overpredicted the maximum pressure in region 2 and the peak pressure in region 3. However, the ZSGS RSTM model predicted peak pressure values in region 3 that were much closer to the experimental data than did either the ZSGS K–ϵ or the Jones–Launder K–ϵ models. None of the predicted values from the models were in good agreement with the experimental data in regions 4 and 5. However, in this region, the predicted values of the Jones–Launder model were in better agreement with experimental values than the results of either ZSGS model.

The tendency of the ZSGS models to perform better at lower pressure ratios and the Jones–Launder K–ϵ model to perform better at higher pressure ratios is further illustrated in Fig. 5a. This figure is a plot of the boundary-layer separation distance from the jet x_{sep} vs p_{jet}/p_∞. Consistent with the methodology used by Aso et al., the location of x_{sep} can be approximated by the intersection of a line drawn tangent to the data defining region 1 with the line $p_{\text{wall}} = p_\infty$. It is clearly seen in Fig. 5a that for the two lower pressure ratios the ZSGS models accurately predicted the experimentally observed separation point to within 5% for the ZSGS RSTM and within 10% for the

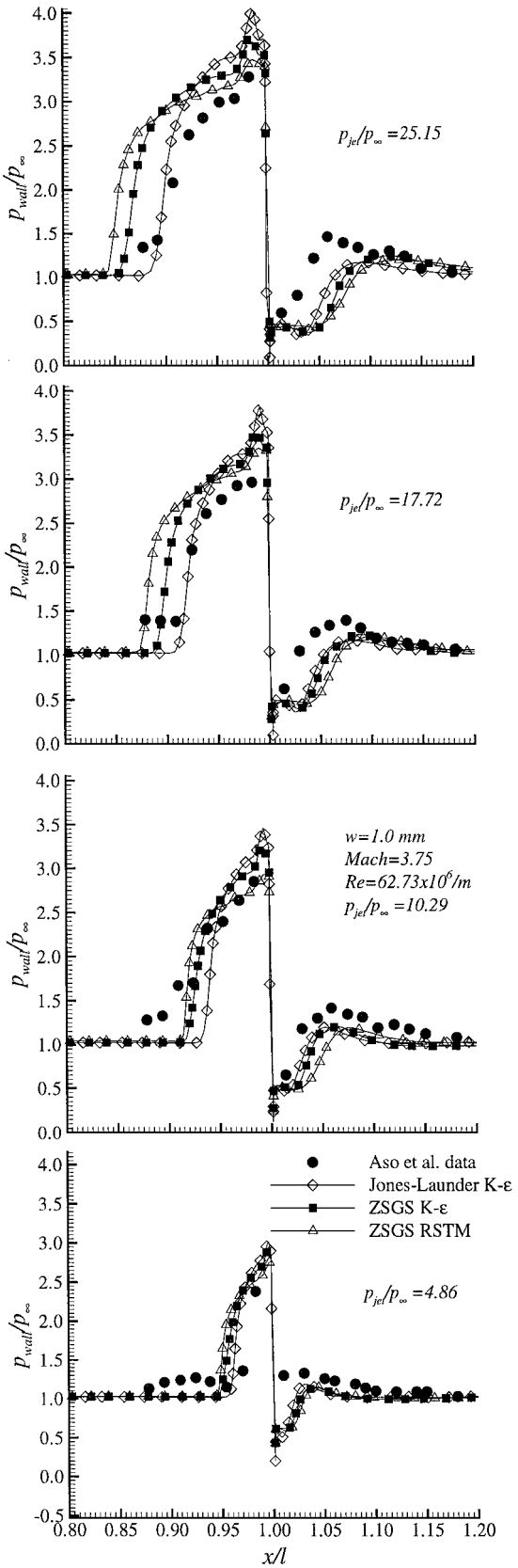

Fig. 4 Comparison of surface pressure profiles for Aso et al.[9] configuration.

ZSGS $K-\epsilon$ model, whereas the predictions by the Jones–Launder $K-\epsilon$ model at these two pressure ratios had differences from the experimental data of 18% or more. At the higher pressure ratios, the results of both ZSGS models became progressively poorer, whereas the results of the Jones–Launder model improved slightly.

Also shown in Fig. 5a is a comparison of the jet plume height h vs p_{jet}/p_∞. Plume heights for the Jones–Launder model were reported by Rizzetta,[2] and experimental data were reported by Aso et al.[9]

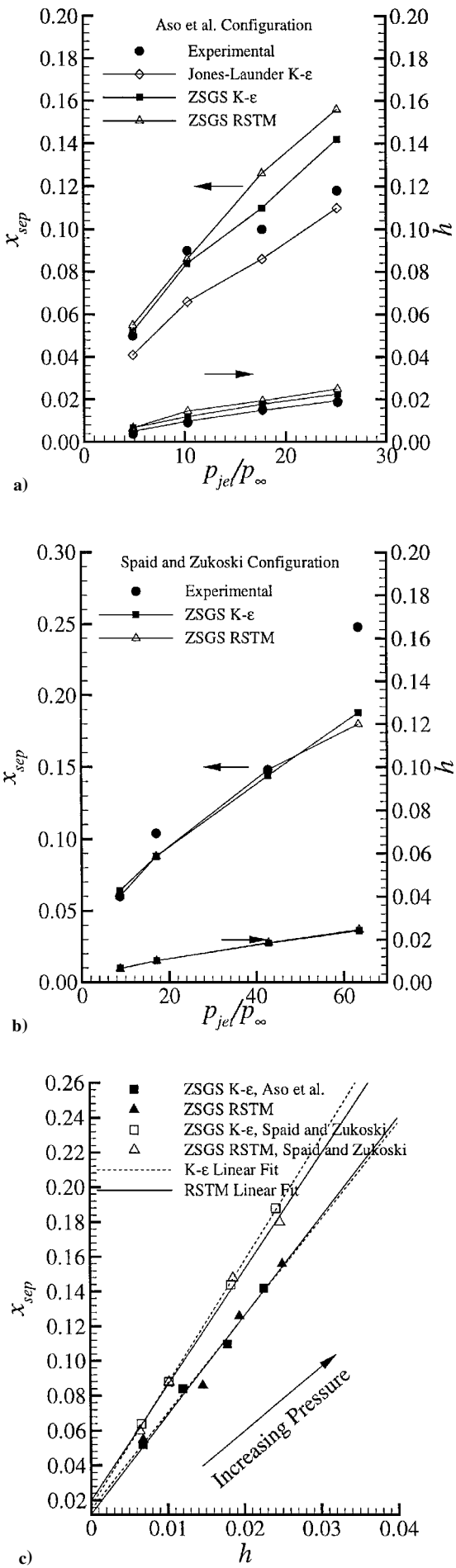

Fig. 5 Separation length and plume height as a function of static pressure ratio.

These results were compared with the numerical results of the two ZSGS models in Fig. 5a. The Jones–Launder model results were nearly identical to the experimental data, whereas the differences from the experimental results for the two ZSGS models ranged from 95 to 135%. The large discrepancies of the ZSGS models may be a result of the ambiguity of how the plume height was measured. Although not explicitly stated, Aso et al.[9] implied through their Fig. 5 that h is defined as the point where the sonic surface upstream of the jet intersects the Mach disk of the jet plume. This location is not necessarily a well-defined point.

2. Spaid and Zukoski Configuration

Numerical simulations of the mean flow conditions listed in Table 1 for Spaid and Zukoski's[8] configuration were also performed with the ZSGS RSTM and ZSGS $K-\epsilon$ turbulence models. Spaid and Zukoski's[8] data provide a better representation of the surface conditions than the data reported by Aso et al.[9] By using 92 pressure taps, Spaid and Zukoski captured the pressure spike in region 3 for all but the lowest pressure ratio (8.743) and captured the pressure well in region 4 at all four pressure ratios. As evidenced by the smooth transition from the undisturbed freestream flow to the jet-induced boundary-layer separation region, the upstream flowfield appears to be fully turbulent and free of shock/boundary-layer interactions.

Numerically obtained surface static pressure distributions and experimental data for the four pressure ratios listed in Table 1 are compared with each other in Fig. 6. The computational results of the two ZSGS models compare very well with the experimental data at the three lower pressure ratios. At pressure ratios of 8.743 and 17.117, the RSTM results are nearly identical to experimental results, and $K-\epsilon$ results are within 10% of experimental data at any given location. However, as with Aso et al.'s configuration, differences between the numerical results and experimental data become larger as the pressure ratio increases. At a pressure ratio of 42.79, both models begin to significantly overpredict the pressure in regions 2 and 3—as much as 9% for the RSTM at the pressure peak and 18% for the $K-\epsilon$ model at the peak. However, both models continue to have good agreement with experimental pressure data in regions 4 and 5. At a pressure ratio of 63.5, the accuracy of the predicted location for boundary-layer separation upstream of the jet begins to deteriorate, and both models significantly overpredict the pressure in regions 2 and 3. Furthermore, the numerical predictions downstream of the jet (regions 4 and 5) begin to differ from the experimental results. As with the lower pressure ratios, the RSTM predictions have better agreement with experimental values than do the $K-\epsilon$ predictions in the flowfield regions upstream of the jet. However, in the flowfield regions downstream of the jet, $K-\epsilon$ predictions are in better agreement with experimental values than are the RSTM predictions for both of the higher pressure ratios.

As with the Aso et al.[9] configuration, the tendency of the ZSGS models to perform better at lower pressure ratios is further illustrated in Fig. 5b by plotting the boundary-layer separation distance from the jet x_{sep} against p_{jet}/p_∞ and by plotting the jet plume height h against p_{jet}/p_∞. At the three lower pressure ratios, the predicted and experimentally determined boundary-layer separation points are very nearly the same, within 15% for both models. However, at the pressure ratio of 63.5, both model's predictions of x_{sep} are relatively poor; differences are within 24% for RSTM and 28% for $K-\epsilon$. Also seen in Fig. 5b is the predicted plume height for the two models. The predictions are nearly identical, but no experimental data on this parameter were reported by Spaid and Zukoski.[8]

Over the course of their experiments, Spaid and Zukoski[8] made the observation that the boundary-layer separation distance is about four plume heights upstream of the jet. This phenomenon is also observed in the numerical results for both of the ZSGS models and in both of the experimental configurations and is illustrated in Fig. 5c. This figure is a plot of x_{sep} vs h for the ZSGS RSTM and ZSGS $K-\epsilon$ model for the two configurations examined along with a linear fit of the computational data at each of the four pressure ratios. Table 2 lists the slope of this linear fit and shows that the computational results are consistent with Spaid and Zukoski's observation. Note that the RSTM results are closer to four for both configurations.

Table 2 Slope of x_{sep}/h linear fit

Model	Spaid and Zukoski[8]	Aso et al.[9]
ZSGS RSTM	4.13	3.73
ZSGS $K-\epsilon$	4.41	3.55

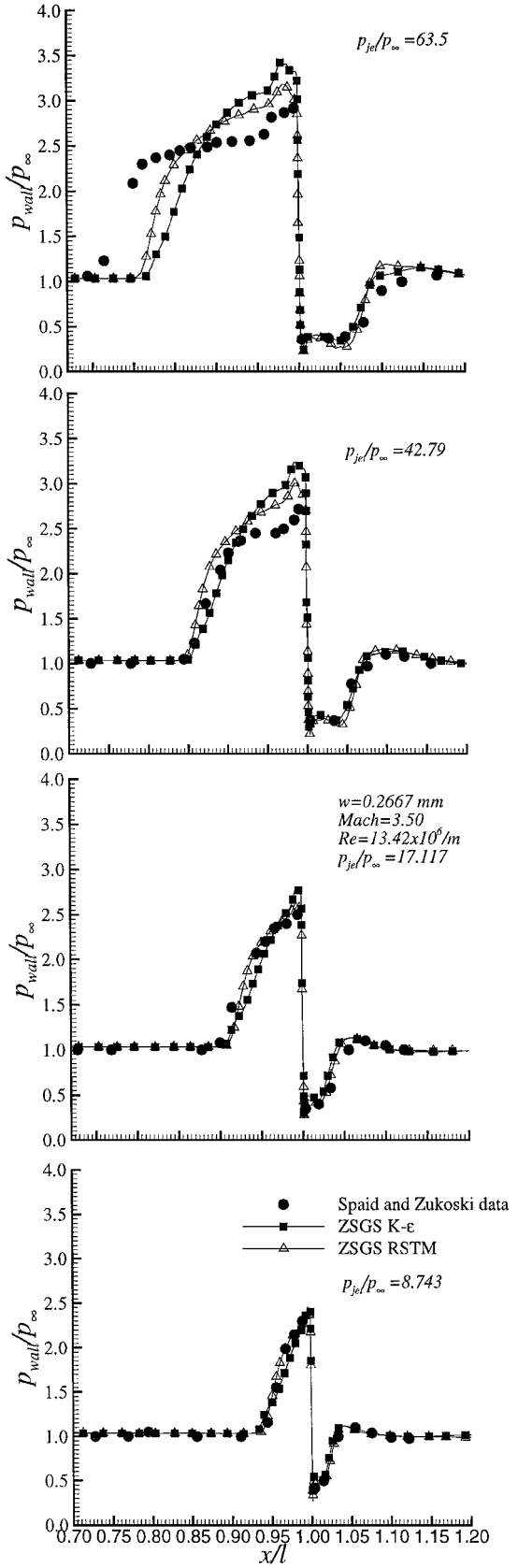

Fig. 6 Comparison of surface pressure profiles for Spaid and Zukoski[8] configuration.

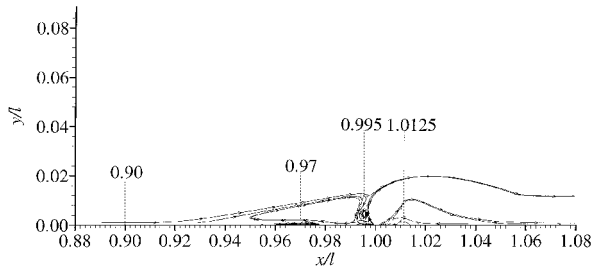

Fig. 7 Location of cross-sectional data samples relative to particle paths.

C. Turbulence Data

It was seen earlier that K–ϵ models are generally satisfactory for the computation of surface pressure values; however, turbulent quantities are also of significant interest because they directly affect heat transfer rates and shear forces. Therefore, predicted values of selected flow variables and derived quantities from the ZSGS K–ϵ model will be compared with those predicted by the ZSGS RSTM. Hence, the ensuing discussion compares and contrasts the features of predicted flowfields generated by the two turbulence models under consideration here. Initially, law-of-the-wall comparisons of predicted u^+ and y^+ values to theoretical values are discussed. This is followed by a discussion of cross-sectional shear-stress profiles from streamwise stations representing characteristic flowfield structures. These streamwise stations, shown in Fig. 7, encompass flat plate turbulent flow conditions upstream of the jet, vortex and shock/boundary-layer interactions upstream of the jet, and vortex/jet wake interactions downstream of the jet. Next, contour plots of the shear stresses, the z component of vorticity ω_z, and the ratio of turbulent kinetic energy to the total energy in the region surrounding the jet are discussed.

Of the simulations discussed in the preceding section, the best agreement with experimental data is obtained for the Spaid and Zukoski configuration with $p_{\text{jet}}/p_\infty = 17.117$; therefore, this configuration is used as a basis for comparison between the ZSGS K–ϵ model and the ZSGS RSTM.

The ZSGS wall-bounded turbulence models have been extensively validated for flat plate law-of-the-wall predictions by Zhang et al.[5,24] Additional validation of the ZSGS models, as implemented in the Fortran code ISAAC, has been performed by Morrison[16,26] and Morrison et al.[6] with comparisons of predicted values of u^+ and y^+ to theoretical values using van Driest II coordinate transformations. Morrison's results for flat plate, turbulent flow conditions were confirmed in this study by comparing the predicted values of u^+ and y^+ with theoretical values using Spalding's buffer layer formula[35] and White's compressibility correction formula[36] for values of $\kappa = 0.41$ and $B = 5.0$. In this comparison, data at a station upstream of the jet and prior to boundary-layer separation ($x/l = 0.9000$) are used. Predictions from both ZSGS models are within 6% of the theoretical values based on the κ and B values used; therefore both ZSGS models are considered valid for the limited range of flow conditions that correspond to flat plate flowfields.

Profiles of the two-dimensional Favre-averaged Reynolds shear stresses are presented in the next four figures. Here it is seen that the RSTM is generally more responsive than the K–ϵ model to the rapid changes in velocity and pressure that occur at the interfaces of the various flow structures.

The first set of profile data examined is taken from station $x/l = 0.9000$ and is reported in Fig. 8a. The flowfield at this station is a fully turbulent, flat plate flow, and predicted values of τ_{xy} from both two models are nearly identical. This should not be surprising because most turbulence models are designed to match τ_{xy} data in the flat plate region of a flowfield. However, predicted values for τ_{xx} and τ_{yy} from the two models differ by more than 100% near the wall. In particular, the peak predicted value of τ_{xx} from the RSTM has a greater magnitude than the peak value predicted by the K–ϵ model, whereas the opposite is true of τ_{yy} at this station. The predicted values of the shear stresses from the RSTM seen here are consistent with the results reported by Morrison[16] and Morrison et al.[6] for flat plate flows.

The second data set examined is the shear stress profiles associated with the vortices found at station $x/l = 0.9700$ (Fig 8b). At this

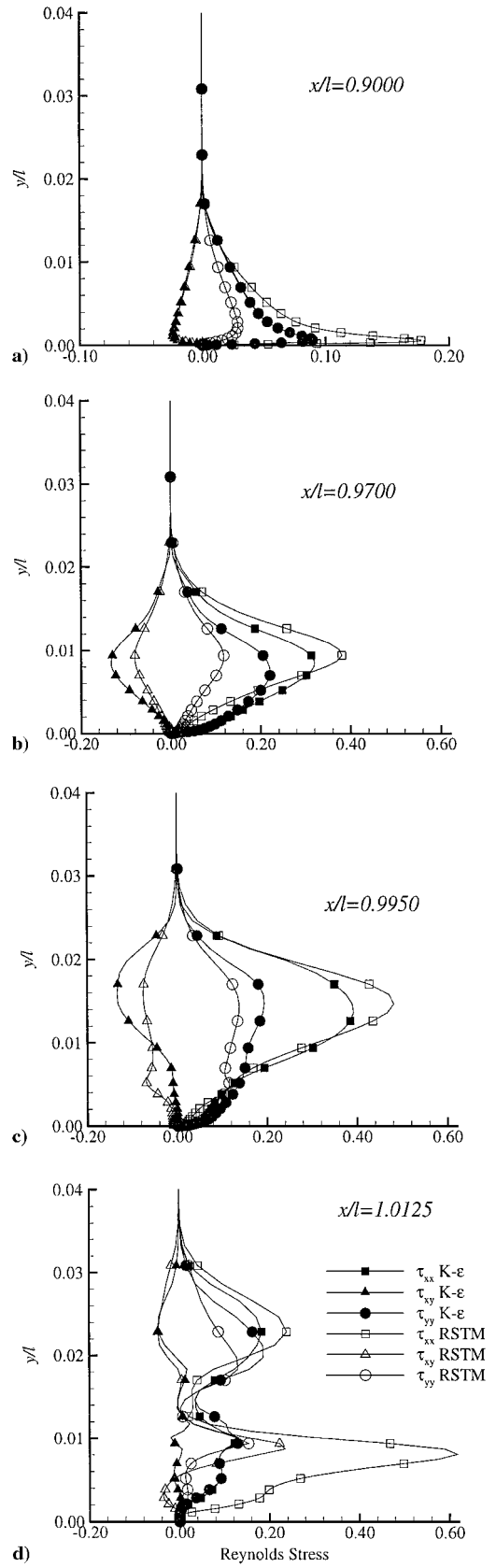

Fig. 8 Comparison of Reynolds stress profiles.

station, the RSTM predicts two vortices stacked on top of each other, a primary clockwise rotating vortex and a tertiary counterclockwise rotating vortex, whereas the K–ϵ model predicts a single primary clockwise rotating vortex. The peaks in the stress profiles correspond to the interface between the primary vortex and the freestream flow. At this interface there is a shock where the flow changes from supersonic to subsonic conditions as the wall is approached. Although the shear stress profiles predicted by the two models are qualitatively

similar, there are significant quantitative differences within the vortices. The peak value predicted for τ_{xx} by RSTM is 18% greater than that predicted by the K–ϵ model, whereas the peak values predicted for τ_{xy} and τ_{yy} by the K–ϵ model are 62 and 83% greater in magnitude, respectively, than those predicted by the RSTM.

The third set of data presented is the shear stress profiles at station $x/l = 0.9950$. The multiple inflections in the shear stress profiles seen in Fig. 8c are caused by changes in flow velocity and pressure gradients in the different flow structures. The peak in the data at $y/l = 0.008$ occurs at the interface of the counterclockwise rotating vortex and the upper edge of the clockwise rotating vortex upstream of the jet, whereas the peak at $y/l = 0.014$ corresponds to the interface between the vortices and the freestream flow. The K–ϵ model predicted minimal changes in the magnitude of the shear stresses at the interface of the two vortices, whereas the RSTM predicted small but noticeable differences in τ_{xy} and τ_{yy} at the interface. As with the K–ϵ model, the RSTM predicted only minimal changes in τ_{xx} at the vortex interface. Across the sonic surface interface, the shear stress profiles exhibited behavior similar to that seen at the sonic surface at station $x/l = 0.9700$.

The final set of profile data examined corresponds to streamwise station $x/l = 1.0125$. The shear stress profiles for this station are shown in Fig. 8d. At this station the data sample crosses three flow structure interfaces at y/l of 0.002, 0.01, and 0.018. Respectively, these are the interfaces between a weak counterclockwise and a strong clockwise rotating vortex, the primary downstream vortex and the lower portion of the jet wake (downstream sonic surface), and the upper portion of the jet wake and the freestream flow. The data at the interface of the jet wake and the freestream flow are similar in form to the data presented in previous figures for the interface of the freestream and a vortex as are the data at the interface between the two vortices at $y/l = 0.002$. However, at the interface of the downstream vortex and the downstream sonic surface, the peak predicted values and rate of response to changing flow conditions is significantly different. At the previous interfaces examined, the flow direction has predominately been from left to right or right to left; however, at this interface the flow direction is predominately from bottom to top. This change in flow direction and the pressure gradient associated with the crossing of a shock apparently has a significant effect on the velocity pressure-gradient correlation tensor Π_{ij} and the turbulence dissipation-rate tensor ϵ_{ij} found in Eq. (5) of the RSTM. It was seen in Sec. II.B that Π_{ij} is not modeled in Eq. (21) of the K–ϵ model because Π_{ij} is a second-order term and that isotropic turbulence is assumed in the K–ϵ model; thus the turbulence dissipation-rate tensor is modeled as $\epsilon_{ij} = \frac{2}{3}\epsilon\delta_{ij}$. These two limitations causes the K–ϵ model to respond slowly or not at all to flow conditions that excite the velocity pressure-gradient correlation tensor and the off-diagonal terms of ϵ_{ij}.

Based on the data provided in the turbulence profiles, it can be concluded that both models satisfy the law-of-the-wall validity test for flat plate flows. Furthermore, outside the recirculation zones and in regions of the flow where the velocity and pressure gradients are small, the two models predict similar values for the shear stresses. However, in regions where the velocity and pressure gradients are not small, i.e., across shocks and wake/freestream interfaces, the models predict significantly different values for the shear stresses. It is assumed that the isotropic turbulence assumption and the lack of the second-order term Π_{ij} in the turbulent kinetic energy equation is the cause of the large disparity in peak values of the shear stresses.

The profiles presented in the preceding discussion provide many pertinent details of the flowfields, but they are only localized descriptions of one particular point in the flowfield. The contour plots seen in Figs. 9–11 provide a more global characterization of how the shear stresses behave around the jet. These contour plots encompass an area starting $x/l = 0.96$, close to the boundary-layer separation point, and extending to $x/l = 1.06$, near the boundary-layer reattachment point, in the streamwise direction and in the transverse direction from $y/l = 0.00$ at the lower wall surface to $y/l = 0.04$, a point close to freestream flow conditions. The contour plots on the left-hand side of the figures represent the ZSGS RSTM results and the contour plots on the right-hand side of the figures display the ZSGS K–ϵ model results (note the jet nozzle is at the center of the figure for both contour plots and that the y coordinate of one plot is the mirror image of the other).

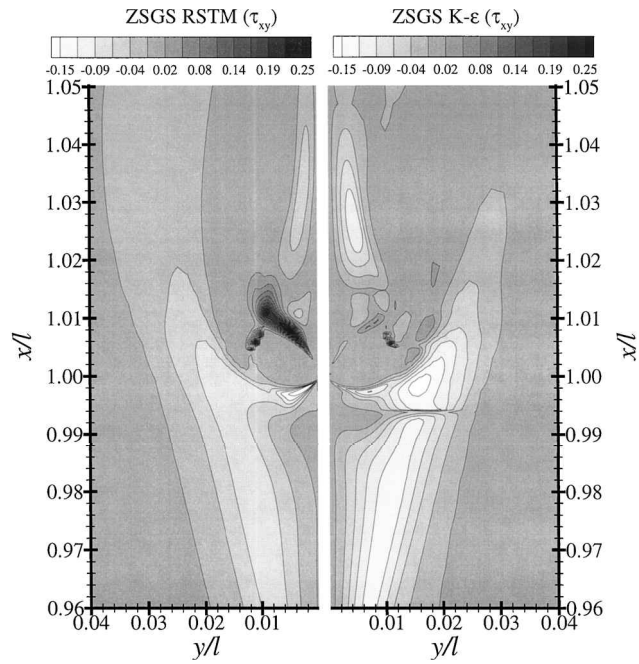

Fig. 9 Comparison of τ_{xy} contours.

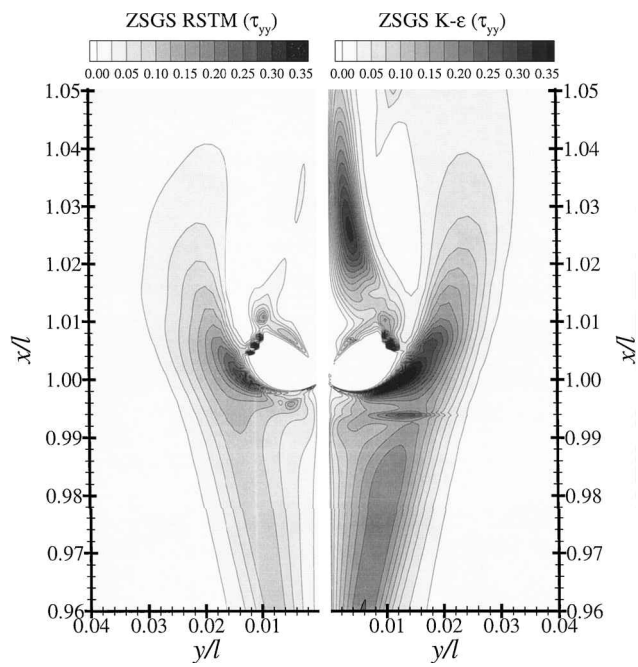

Fig. 10 Comparison of τ_{yy} contours.

Contour plots of τ_{xy} for both turbulence models are presented in Fig. 9. Immediately seen in the contours of the RSTM is the smooth transition from one shear stress level to another. This is in marked contrast to the K–ϵ model predictions. The K–ϵ model predictions exhibit a discontinuous distribution of shear stress upstream of the jet and patchy island-type distribution of shear stress downstream of the jet. The discontinuities in the K–ϵ model are most apparent upstream of the jet at $x/l = 0.994$. The discontinuity at $x/l = 0.994$ can be traced to the wall damping function f_μ, [Eq. (19)] used to compute the turbulent eddy viscosity μ_t in Eq. (18). The turbulent eddy viscosity is, in turn, used in the constituent relationship that is used to compute τ_{ij} [Eq. (22a)].

For wall-bounded flows, f_μ is required to maintain asymptotic consistency of the K and ϵ equations as the surface is approached. For flat plate attached boundary-layer flows, f_μ is tailored to approach unity as $y \to \delta$, where δ is the boundary-layer thickness.

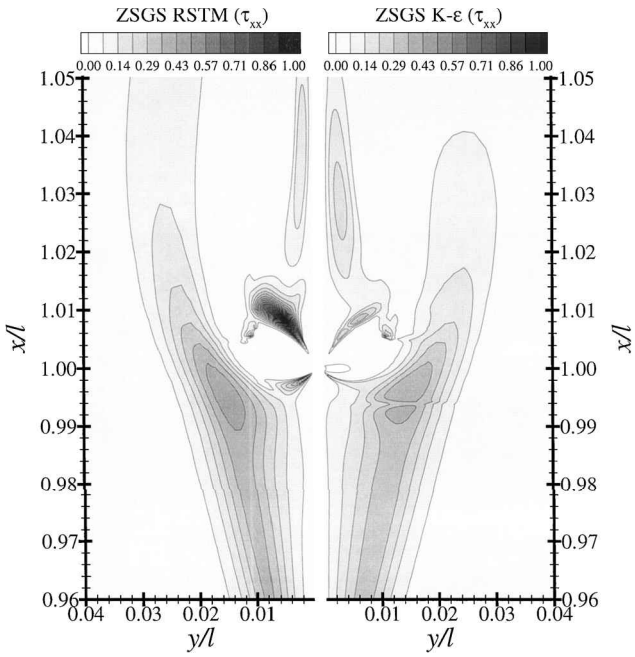

Fig. 11 Comparison of τ_{xx} contours.

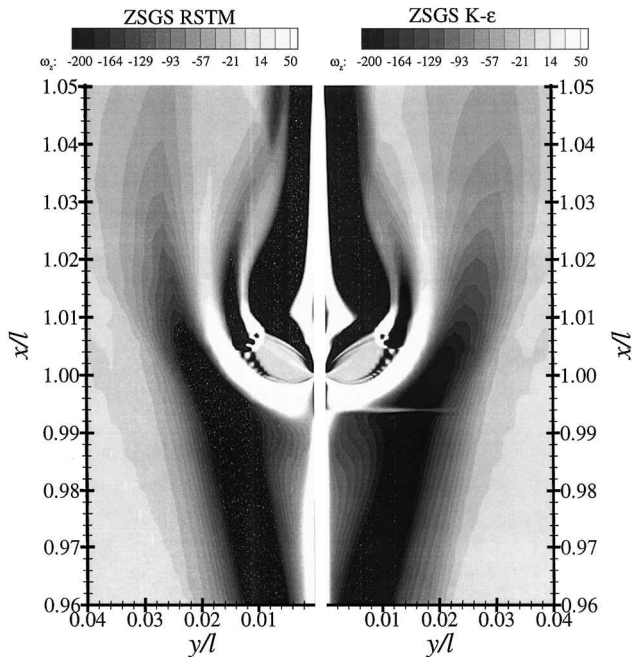

Fig. 12 Comparison of ω_z contours.

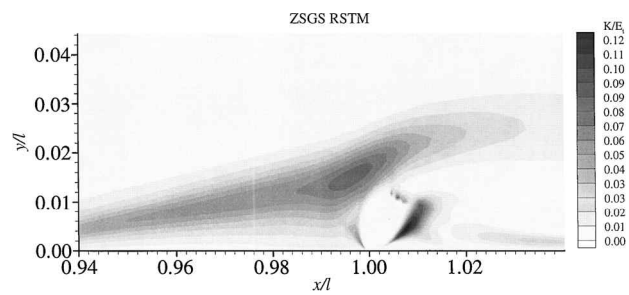

Fig. 13 Fraction of E_t composed of K.

The rate at which $f_\mu \to 1$ is largely governed by the magnitude of the viscous shear stress at the wall, $\tau_w = \mu \partial u/\partial y|_{y=0}$. The viscous shear stress at the wall is normally somewhat larger than unity at the plate surface, and generally, the larger $\partial u/\partial y|_{y=0}$ is, the faster $f_\mu \to 1$ as $y \to \delta$. However, for recirculating flows and stagnation points, there is a point on the plate surface where $\partial u/\partial y|_{y=0} \approx 0$. In the neighborhood of this point $\partial u/\partial y|_{y=0} \ll 1$, implying locally that $\tau_w \ll 1$, causing f_μ to approach unity much slower than it would for a flat plate boundary layer. Thus, the damping needed to preserve asymptotic consistency of the K–ϵ model equations adversely affects computations far away from the wall at separation and stagnation points.

The degree to which the flowfield away from the wall is affected is determined by the size of the separation or stagnation point. In other words, at a location where the flow is primarily moving horizontally to the surface and a separation bubble occurs, there is likely to be only a small region where the flow is normal to the surface at the surface. However, at a location where the predominate flow direction is normal to the surface, a large stagnation region forms where there are numerous surface locations with $\partial u/\partial y \approx 0$, thus having an impact on a large region of the flow.

Consider flow conditions at station $x/l = 0.994$. At this station the two strong upstream vortices have a common interface where from Fig. 7 one can see that the flow at this station is predominately normal to the surface from $y/l = 0.01$ all the way down to the surface of the plate. This flow condition forms a large stagnation region where $\partial u/\partial y|_{y=0} \approx 0$ at many of the surrounding surface locations, thereby adversely impacting computations of turbulent quantities well beyond the boundary layer.

Although the same stagnation conditions are present in the flowfield predicted by the RSTM, the discontinuity in the turbulent quantities is not present because the RSTM does not use the eddy viscosity model to compute the shear stress. The RSTM treats the shear stresses as one of the conserved variables and solves for them as it would for a mean flow variable.

Contour plots for τ_{yy} and τ_{xx} are shown in Figs. 10 and 11, respectively. These contour plots verify that the discontinuity seen at $x/l = 0.994$ in Fig. 9 is present in all the shear stress contour plots of the K–ϵ model results. Because the turbulence model equations and the mean flow equations are strongly coupled through the equation of state, it is reasonable to expect the discontinuity seen in the shear stress contours to have an influence on other flow variables. This assumption is verified in Fig. 12, which shows a contour plot of the z component of vorticity, where $\omega_z = \partial u/\partial y - \partial v/\partial x$. From this plot it is clear that the eddy viscosity model affects the mean flow variables as well as the turbulent shear stresses. The K–ϵ results indicate the vorticity anomaly at $x/l = 0.994$ is also found for each of the conserved mean flow variables.

Often when a laminar Navier–Stokes solver is modified to include a turbulence model, the contribution of K to the total energy term E_t is neglected. Huang and Coakley[37] did a comparative study with a hypersonic cylinder flare to determine the effects of neglecting K in E_t. Their results show a decrease of 9% in peak surface pressure when K is accounted for in the total energy term.

Results from the current study of a jet injection flowfield are similar to those of Huang and Coakley. Rizzetta's Jones–Launder model results for the Aso et al. configuration were performed without K contributing to E_t (Ref. 2), whereas the current computations with the ZSGS K–ϵ model accounted for the contribution of K to E_t. A comparison of the results of the two computations is seen in Fig. 4. As with Huang and Coakley's[37] results, the model accounting for K has a lower peak surface pressure than the model that does not account for K. Some insight as to why the peak surface pressure is different for the two sets of computational results is provided by Fig. 13. This figure shows that in the regions just upstream and downstream of the jet, K accounts for as much as 12% of E_t.

VI. Conclusions

A comparative study was computed to evaluate the relative performance of the ZSGS second-order turbulence model and the ZSGS and Jones–Launder K–ϵ models for shock/boundary-layer interactions resulting from sonic slot injection at the surface of a flat plate in a supersonic freestream. A mesh step-size study indicated the adequacy of numerical resolution for the present application. Eight cases were examined, comprising two different experimental configurations and four different pressure ratios for each configuration.

Surface static pressure distributions computed with the ZSGS RSTM and the ZSGS K–ϵ model for the Spaid and Zukoski

configuration compared very well for the three lower-pressure ratios examined. Furthermore, good agreement between the computed separation length and the experimentally obtained values at the three low-pressure ratios was observed. Only at the largest pressure ratio did the ZSGS models start to predict significantly different results from the experimental data.

This disparity may be a result of a lack of knowledge of the turbulence properties at the nozzle exit or a result of turbulence model limitations for the overall flowfield at the higher pressure ratios. The simple boundary conditions presented in Sec. IV may remain physically realistic only when conditions at the nozzle exit impact a small domain in the immediate vicinity of the nozzle. For sufficiently large pressure ratios, this situation does not exist.

Taken as a whole, the surface static-pressure distributions computed with all three of the turbulence models for the Aso et al. configuration were marginal at best. In light of the good agreement seen with the Spaid and Zukoski configuration,[8] the poor agreement of computed results to the experimental data of Aso et al.[9] is likely due to three-dimensional effects and leading-edge bluntness, devaluing this data set for turbulence model validation.

Additional evaluation of the turbulence profiles computed for the Spaid and Zukoski configuration[8] indicate that both ZSGS models satisfy the law of the wall for flat plate flows. Furthermore, it is seen that away from flow structure interfaces the two models predict similar values for the shear stresses. However, the models predict significantly different values for the shear stresses in the vicinity of shocks and flow structure interfaces, particularly at interfaces where there are rapid changes in pressure and flow direction. The latter disparity is a result of the K–ϵ formulation not modeling the second-order pressure-velocity-gradient term and the restriction to isotropic turbulence dissipation rates. The contour plots of τ_{ij} and ω_z highlight the nonphysical behavior brought about by the eddy viscosity model used in the K–ϵ formulation at the interface of two strong vortices.

Finally, it was shown that the turbulent kinetic energy accounts for as much as 12% of the total energy in regions with significant shock interaction. Exclusion of K from the total energy equation may account for differences seen in the peak surface pressure predictions from the two K–ϵ models examined.

Acknowledgments

Computational resources used for this study were sponsored by the U.S. Air Force Office of Scientific Research through Task 2300AS (Brian Sanders, Program Manager). The authors are grateful to Rodney Bowersox and Don Rizzetta for their many helpful hints and insights and especially to Joseph Morrison, the developer of the program ISAAC, whose extensive help in setting up the code and in interpreting results is incalculable.

References

[1]Northam, G., and Anderson, G., "Supersonic Combustion Ramjet Research at Langley," AIAA Paper 86-0159, Jan. 1986.

[2]Rizzetta, D., "Numerical Simulation of Slot Injection into a Turbulent Supersonic Stream," AIAA Paper 92-0827, Jan. 1992.

[3]Gerlinger, P., Algermissen, J., and Bruggemann, D., "Simulation of Turbulent Slot Injection of Different Gases into a Supersonic Air Stream," AIAA Paper 94-2247, June 1994.

[4]Wilcox, D., *Turbulence Modeling for CFD*, DCW Industries, Inc., La Cañada, CA, 1993, Chap. 4.

[5]Zhang, H., So, R., Gatski, T., and Speziale, C., "A Near-Wall Second-Order Closure for Compressible Turbulent Flows," *Near-Wall Turbulent Flows*, edited by R. So, C. Speziale, and B. Launder, Elsevier, New York, 1993, pp. 209–218.

[6]Morrison, J., Gatski, T., Sommer, T., Zhang, H., and So, R., "Evaluation of a Near-Wall Turbulent Closure Model in Predicting Compressible Ramp Flows," *Near-Wall Turbulent Flows*, edited by R. So, C. Speziale, and B. Launder, Elsevier, 1993, New York, pp. 239–250.

[7]Settles, G., and Dodson, L., "Hypersonic Turbulent Boundary-Layer Interaction Database," NASA CR-177577, April 1991.

[8]Spaid, F., and Zukoski, E., "A Study of the Interaction of Gases Jets from Transverse Slots with Supersonic External Flows," *AIAA Journal*, Vol. 6, No. 2, 1968, pp. 205–212.

[9]Aso, S., Okuyama, S., Kawai, M., and Ando, Y., "Experimental Study on the Mixing Phenomena in Supersonic Flows with Slot Injection," AIAA Paper 91-0016, 1991.

[10]Jones, W., and Launder, B., "The Prediction of Laminarization with a Two-Equation Model of Turbulence," *International Journal of Heat and Mass Transfer*, Vol. 15, Jan. 1972, pp. 301–314.

[11]Sterett, J., and Holloway, P., "On the Effect of Transition on Parameters Within a Separated Region at Hypersonic Speeds—with Emphasis on Heat Transfer," *Symposium on Fully Separated Flows*, American Society of Mechanical Engineers, New York, 1964, pp. 15–26.

[12]Sarkar, S., "Modeling the Pressure-Dilatation Correlation," Inst. for Computer Applications in Science and Engineering, ICASE Rept. 91-42, NASA Langley Research Center, Hampton, VA, May 1991.

[13]Speziale, C., "Analytical Methods for the Development of Reynolds-Stress Closures in Turbulence," *Annual Review of Fluid Mechanics*, Vol. 23, 1991, pp. 107–157.

[14]Vandromme, D., and HaMinh, H., "About the Coupling of Turbulence Closure Models with Averaged Navier–Stokes Equations," *Journal of Computational Physics*, Vol. 65, No. 2, 1986, pp. 386–409.

[15]Speziale, C., and Sarkar, S., "Second-Order Closure Models for Supersonic Turbulent Flows," AIAA Paper 91-0217, 1991.

[16]Morrison, J., "A Compressible Navier–Stokes Solver with Two-Equation and Reynolds Stress Turbulence Closure Models," NASA CR-4440, May 1992.

[17]Morkovin, M., "Effect of Compressibility on Turbulent Flow," *The Mechanics of Turbulence*, edited by A. Favre, Gordon and Beach, New York, 1964, pp. 367–380.

[18]Launder, B., Reece, G., and Rodi, W., "Progress in the Development of a Reynolds-Stress Turbulence Closure," *Journal of Fluid Mechanics*, Vol. 68, Jan. 1975, pp. 537–566.

[19]Lai, Y., and So, R., "On Near-Wall Turbulent Flow Modeling," *Journal of Fluid Mechanics*, Vol. 221, Jan. 1990, pp. 641–673.

[20]Zhang, H., So, R., and Zhu, M., "A Near-Wall Second-Order Turbulence Model for Wall-Bounded Flows," *Ninth Symposium on "Turbulent Shear Flows,"* Springer–Verlag, New York, 1993, Chap. 8, pp. 2.1–2.6.

[21]So, R., Lai, Y., Zhang, H., and Hwang, B., "A Review of Near-Wall Reynolds-Stress Closures," NASA CR-4369, Jan. 1991.

[22]Sarkar, S., Erlebacher, G., and Hussaini, M., "Direct Simulation of Compressible Turbulence in a shear Flow," Inst. for Computer Applications in Science and Engineering, ICASE Rept. 91-29, NASA Langley Research Center, Hampton, VA, March 1991.

[23]Cebeci, T., and Smith, A., *Analysis of Turbulent Boundary Layers*, Academic, New York, 1974, Chap. 4.

[24]Zhang, H., So, R., Speziale, C., and Lai, Y., "A Near-Wall Two-Equation Model for Compressible Turbulent Flows," AIAA Paper 92-0442, Jan. 1992.

[25]Sarkar, S., Erlebacher, G., Hussaini, M., and Kreiss, H., "The Analysis and Modeling of Dilatational Terms in Compressible Turbulence," *Journal of Fluid Mechanics*, Vol. 227, 1991, pp. 473–493.

[26]Morrison, J., "Flux Difference Split Scheme for Turbulent Transport Equations," AIAA Paper 90-5251, Oct. 1990.

[27]VanLeer, B., "Toward the Ultimate Conservative Difference Schemes V. A Second Order Sequel to Godunov's Method," *Journal of Computational Physics*, Vol. 32, No. 1, 1979, pp. 101–136.

[28]Roe, P., "Approximate Riemann Solvers, Parameter Vectors, and Difference Schemes," *Journal of Computational Physics*, Vol. 43, No. 2, 1981, pp. 357–372.

[29]Venkatakrishnan, V., "Preconditioned Conjugate Gradient Methods for the Compressible Navier–Stokes Equations," *AIAA Journal*, Vol. 29, No. 7, 1991, pp. 1092–1100.

[30]Chakaravarthy, S., Szema, K., Goldberg, U., Gorski, J., and Osher, S., "Application of a New Class of High Accuracy TVD Schemes to the Navier–Stokes Equation," AIAA Paper 85-0165, 1985.

[31]Swanson, R., and Turkel, E., "A Multistage Time-Stepping Scheme for the Navier–Stokes Equations," AIAA Paper 85-0035, 1985.

[32]Abbett, M., "Boundary Condition Calculation Procedures for Inviscid Supersonic Flow Fields," *Proceedings of the AIAA Computational Fluid Dynamics Conference*, AIAA, New York, 1973, pp. 153–172.

[33]Steinbrenner, J., and Chawner, J., "The GRIDGEN Version 9: Multiple Block Grid Generation Software," MDA Engineering, Inc., MDA Engineering Rept. 94-01, Arlington, TX, Aug. 1994.

[34]Vinokur, M., "On One-Dimensional Stretching Functions for Finite-Difference Calculations," *Journal of Computational Physics*, Vol. 50, No. 3, 1983, pp. 215–234.

[35]Spalding, D., "A Single Formula for the Law of the Wall," *Journal of Applied Mechanics*, Vol. 28, No. 3, 1961, pp. 455–457.

[36]White, F., *Viscous Fluid Flow*, 2nd ed., McGraw–Hill, New York, 1991, Chap. 5.

[37]Huang, P., and Coakley, T., "An Implicit Navier–Stokes Code for Turbulent Flow Modeling," AIAA Paper 92-0547, Jan. 1992.

C. G. Speziale
Associate Editor